Modeling of Velocity Distribution Among Microchannels with Triangle Manifolds

Minqiang Pan and Yong Tang
School of Mechanical and Automotive Engineering, South China University of Technology, Guangzhou 510640, P.R. China

Hao Yu and Hongqing Chen
School of Chemistry and Chemical Engineering, South China University of Technology, Guangzhou 510640, P.R. China

DOI 10.1002/aic.11817
Published online June 23, 2009 in Wiley InterScience (www.interscience.wiley.com).

A model of velocity distribution among microchannels with triangle manifolds is proposed. According to the flow behaviors analyzed by Fluent, the manifolds are divided into several approximate rectangular channels, and then an equivalent simplified resistance network model is developed to establish the relationships between the velocities and pressure drops in microchannels and approximate rectangular channels. The velocity distributions are calculated under two situations, respectively, considering and ignoring singular losses. The outcomes of the present study are compared with Fluent's simulated results to analyze the effects of singular losses on the velocity distributions. It indicates that the proposed model is suitable for the calculation of velocity distribution among microchannels with obtuse angled or right triangle manifolds under low Reynolds numbers. The premise of ignoring singular losses is that the frictional pressure drops are three times larger than the singular pressure drops in each flow loop. The manifold optimization results indicate that the velocity distribution among microchannels with right triangle manifolds is much more uniform than that of the corresponding one with obtuse angled manifolds. © 2009 American Institute of Chemical Engineers *AIChE J,* 55: 1969–1982, 2009

Keywords: velocity distribution, laminated microreactor, microchannel array, triangle manifold

Introduction

Microchannel reactors are chemical reaction units with microchannels fabricated by microfabrication technology on the solid surface. Incorporating microchannels offers higher heat and mass transfer rates, as well as higher surface-to-volume ratios, leading to improved process efficiency and smaller reaction volumes. Rapid development of microfabrication technology has enabled microchannel reactors to be gradually applied in the fields of chemistry, chemical engineering, and biotechnology[1] within several years.

The two fundamentally different constructions of microreactors are monolithic construction and laminated-sheet structure. Microchannels or microstructures are incorporated into a single metal[2–4] or silicon block[5,6] by microfabrication methods to form monolithic construction, while multiple metal or silicon sheets, patterned with microchannel array, are first piled up and then welded together to yield a single laminated-sheet component.[7,8] Although the fabrication of monolithic construction is relatively simple, it can only serve a single reaction, and therefore, it is hard to integrate with complicated structures and multiple reactions.

Correspondence concerning this article should be addressed to M. Pan at mqpan@scut.edu.cn.

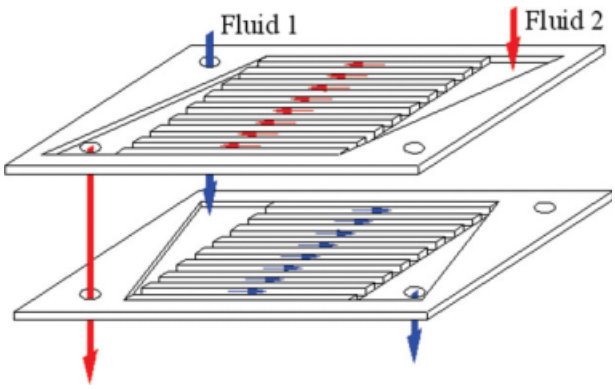

Figure 1. The stacked microchannel sheets with mirror manifolds.

[Color figure can be viewed in the online issue, which is available at www.interscience.wiley.com.]

As laminated-sheet structure enables the coupling of endothermic and exothermic reactions in the same component, and moreover, the number of microchannel sheets can be increased or decreased on the demand of reactions. Laminated-sheet structure is considered as the best solution in terms of satisfying the complex requirements of microreactors.

The fluid velocity distribution among microchannels directly affects the performances of laminated microreactors. Relatively uniform velocity distribution is in favor of improving the heat and mass transfer efficiency and obtaining more even residence time, as well as improving the conversion rate and selectivity of process. Some preliminary theoretical analyses[9,10] on velocity or flow distribution among microchannels have been made. However, only sparse attempts have been reported in the literature concerning on the effects of singular losses on the velocity distribution among microchannels. For the purpose of achieving rapid calculation of fluid velocities, some researchers[10,11] neglected the singular losses among microchannels to obtain linear dependence of pressure drop on the velocity. However, it indicated that the effects of singular losses on total pressure could only be ignored under certain conditions.[12]

The objective of the present work is to develop a theoretical model of velocity distribution among microchannels with triangle manifolds and analyze the effects of singular losses on the velocity distribution. For this purpose, the manifolds are divided into several approximate rectangular channels based on the analysis of pressure distributions in the manifolds by Fluent, and then an equivalent simplified resistance network model is developed to establish the relationships between the velocities and pressure drops in microchannels and approximate rectangular channels. The velocity distributions are calculated under two situations, respectively, considering and ignoring singular losses. The calculation outcomes are compared with Fluent's simulated results to verify the validity of the proposed theoretical model and analyze the effects of singular losses on the velocity distributions. Moreover, the application scope of theoretical model is analyzed, and an optimization method of the manifold shape is proposed.

Microchannel Array Model with Triangle Manifolds

Model structure

Multiple microchannel sheets with mirror manifolds are usually stacked together in a laminated microreactor for the coupling of endothermic and exothermic reactions, therefore, the manifold shape is generally designed to be triangle or trapezoid, leaving other side as the passage for another fluid, as shown in Figure 1.

According to the magnitude of $\angle SC_1C_{N+1}$ of manifolds, the manifolds can be divided into three types, as shown in Figure 2. When the magnitude of $\angle SC_1C_{N+1}$ is more than, equivalent to, or less than 90°, the manifolds here are called obtuse angled triangle, right triangle, or acute triangle manifold, respectively. Among these three types of manifolds, the similar polygon manifolds $SGC_{N+1}C_1(G_0)$ are also included. The polygon manifold is turned into the triangle one when the lengths of GC_{N+1} and G_0C_1 are equivalent to zero.

In the laminated structure as depicted in Figure 1, only a single microchannel sheet is selected to study the characteristics of velocity distribution among microchannels in this work. The velocity distributions in other laminated sheets can be obtained by the change of the flow behaviors, such as entrance velocity and kinetic viscosity. The studied model consists of an inlet, an outlet, parallel microchannels with rectangular cross-sections, and two triangle manifolds: one is inlet manifold and the other is outlet manifold, as shown in Figure 3. The direction of fluid is perpendicular to the inlet and outlet.

Simulation analysis of pressure distributions in the manifolds

Because of irregular manifold shapes, it is difficult to study the flow pattern in the manifolds and it is necessary to simplify the manifolds. Take the obtuse angled triangle manifolds for example, as shown in Figure 2a. First, choose C_1 as the origin of the coordinate system. Then select

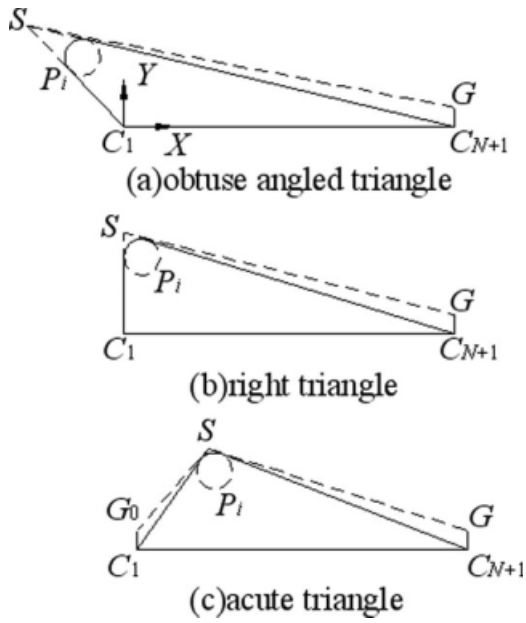

Figure 2. Three different types of manifolds.

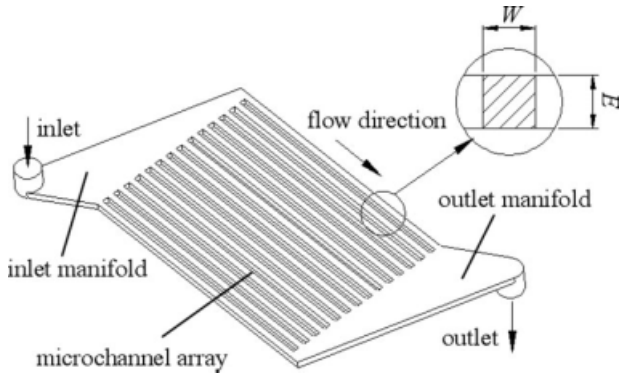

Figure 3. Microchannel array model with triangle manifolds.

C_1C_{N+1} as the axis X and right as positive, while the vertical plumb perpendicular to C_1C_{N+1} as axis Y and up as positive. During the design of the manifold, the lengths of C_1C_{N+1} and GC_{N+1} are first determined, and then the position and magnitude of the inlet P_i are chosen, two tangent lines to the circle P_i through C_1 and G are respectively made, which yields the final manifold shape. The lengths of manifold bottom C_1C_{N+1} and side GC_{N+1} are defined as L_m and H, respectively. And the microchannel number, length, width, depth, and interval are defined as N, L_c, W_c, E, and W_s, respectively.

For the purpose of studying the flow pattern in the manifolds, a special case shown in Table 1 is selected here to analyze the pressure distributions in the inlet and outlet manifolds under different Reynolds numbers based on the inlet diameter. The liquid water (density as 998.2 kg m^{-3} and kinetic viscosity as 1.003×10^{-3} kg m^{-1} s^{-1}) and gaseous water (density as 0.5542 kg m^{-3} and kinetic viscosity as 1.34×10^{-5} kg m^{-1} s^{-1}) under 300 K are selected as the fluid, respectively. The Navier–Stokes equation with non-slip boundary condition and negligible gravity is used to evaluate the flow characteristics.[11] The model was meshed by Cooper scheme type, as depicted in Figure 4. The boundary conditions used are the velocity value in the Z direction of the inlet and the freedom outlet flow. The outlet pressure condition is set to zero and the solid boundaries are stationary. The flow pattern is assumed to be laminar in the microchannels. Segregated manner is selected as solver type.

Table 1. Basic Structural Parameters of the Microchannel Model

Microchannel Structural Parameters				
N	L_c	W_c	E	W_s
20	20 mm	500 μm	500 μm	500 μm
Manifold Structural Parameters				
	H	coordinates of inlet $P_i(X_{pi}, Y_{pi})$		R_{pi}
	2 mm	(−2,7)		2 mm

The simulated results of pressure distributions in the microchannel array model are shown in Figure 5. As presented in the figures, the laws of pressure distributions in the model accord to each other when the liquid water and gaseous water appear the same Reynolds numbers. When the Reynolds number is no more than 300, the pressure contours in the inlet and outlet manifold are approximately parallel to each other, and the directions of pressure contours are perpendicular to the bisector of $\angle C_1SG$. When the Reynolds number surpasses 300, the pressure contours in the inlet manifold become more unparallel with the increasing Reynolds numbers. Because of the coupling between non-linear flow singularities and velocity profiles under development, the pressure contours in the outlet manifold still maintain parallel to each other. The pressure distributions in the right triangle manifolds are similar to those of Figure 5.

Division method of manifolds

The direction of resultant forces affected on the fluid during the flowing process is perpendicular to the isobaric surface and points to the direction of the decreasing pressures, so the manifolds can be divided into multiple flow passages along the direction of the decreasing pressures, and the directions of flow passages are perpendicular to the pressure contours. Since the pressure contours are perpendicular to the bisector of $\angle C_1SG$ under low Reynolds numbers, the divided flow passages are also perpendicular to the bisector of $\angle C_1SG$.

Take the inlet manifold $GT_1T_2C_1C_{N+1}$ for example to introduce the division method of manifolds, as shown in Figure 6. The division method of the outlet manifold is similar

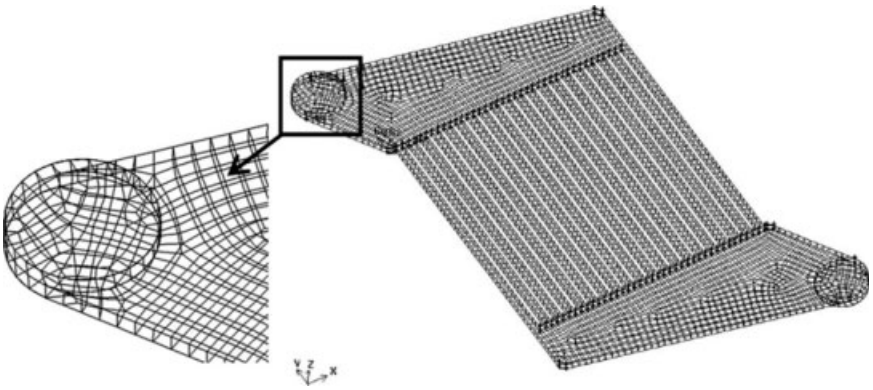

Figure 4. The model meshed by Cooper scheme type.

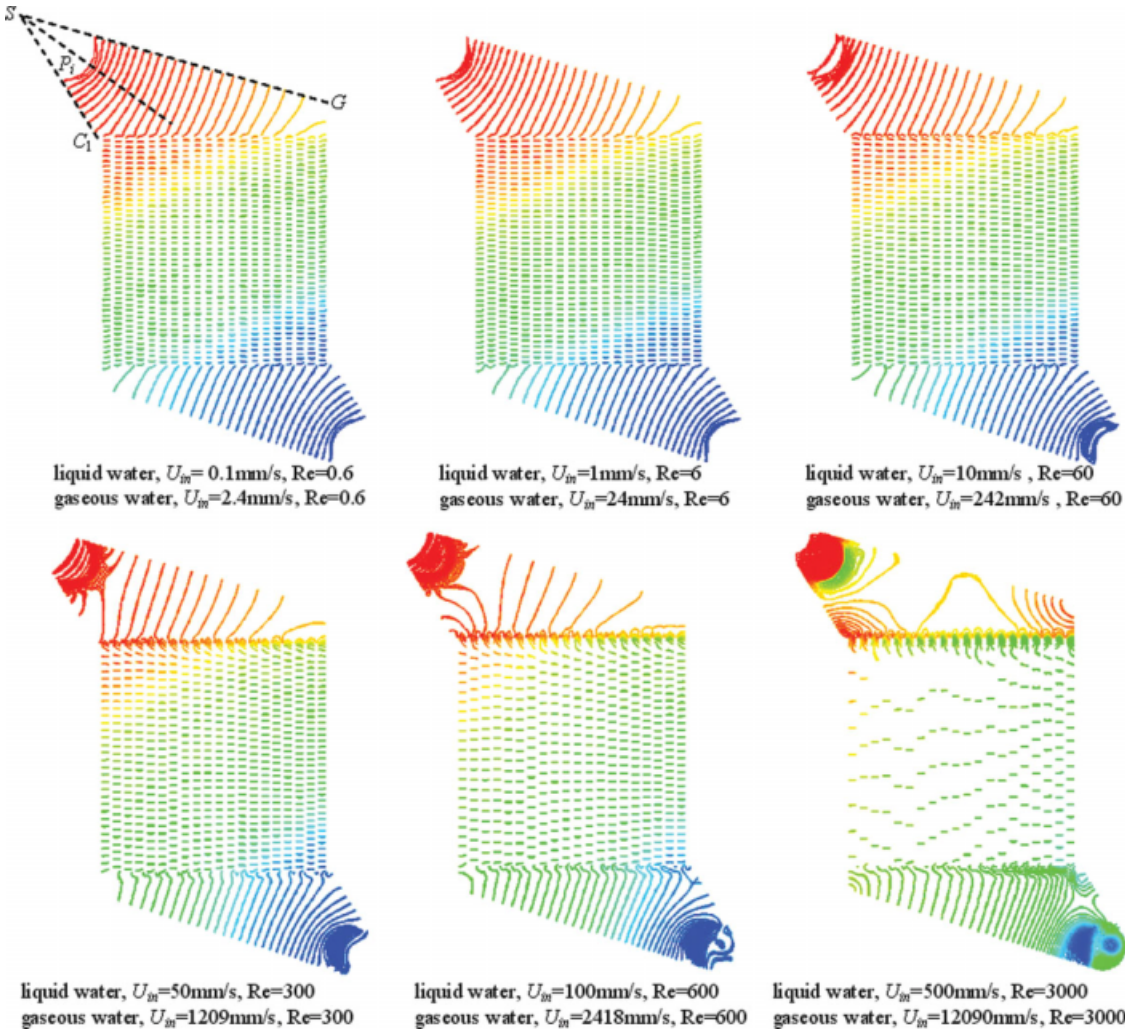

Figure 5. Pressure distributions in the microchannel array model under different Reynolds numbers (U_{in} refers to the entrance velocity).

[Color figure can be viewed in the online issue, which is available at www.interscience.wiley.com.]

to that of the inlet manifold. First, extend the segment GT_1 and C_1T_2 to S, and then draw the bisector SP_i of $\angle GSC_1$. Through C_1, C_1F_1 is drew perpendicular to SP_i and meets the segment SG in F_1, which divides the inlet manifold into two parts: one is the polygon $T_1T_2C_1F_1$ called transition chamber here, and the other is the polygon $C_1C_{N+1}GF_1$ called connected chamber. Then the connected chamber $C_1C_{N+1}GF_1$ is further divided into multiple intervals. Draw C_iF_i (i = 2, 3, …, N) perpendicular to SP_i through C_i (i = 2, 3, …, N), and intersect to the segment GS at F_i (i = 2, 3, …, N), respectively. Through F_i (i = 1, 2, …, $N-1$), draw vertical plumb perpendicular to the segment $C_{i+1}F_{i+1}$ (i = 1, 2, …, $N-1$). Therefore, the connected chamber $C_1C_{N+1}GF_1$ is divided into N intervals, which forms N approximate rectangular channels $C_iC_{i+1}F_{i+1}F_i$ (i = 1, 2, …, N), and the Nth channel $C_NC_{N+1}F_N$ also seems as an approximate rectangular channel here even though it is a triangle channel.

After the microchannel array model being simplified, by the calculation methods presented in Appendix A, the widths and lengths of approximate rectangular channels can be obtained as follows

$$L_{C_iF_i} = \sqrt{(X_{C_i} - X_{F_i})^2 + Y_{F_i}^2} \quad (i = 1, 2, \ldots, N) \tag{1}$$

$$L_{in} = L_m/N \cdot \sin(\arctan k_{C_iF_i}) \tag{2}$$

where

$$\begin{cases} X_{F_i} = \dfrac{k_{SG} \cdot L_m - k_{C_iF_i} \cdot (i-1)\dfrac{L_m}{N} - H_{in}}{k_{SG} - k_{C_iF_i}} \\ Y_{F_i} = \dfrac{-k_{SG}k_{C_iF_i}(i-1)\dfrac{L_m}{N} + k_{SG}k_{C_iF_i}L_m - k_{C_iF_i}H_{in}}{k_{SG} - k_{C_iF_i}} \end{cases} \tag{3}$$

If X_{F_i} (obtained by Eq. 3) > L_m, then

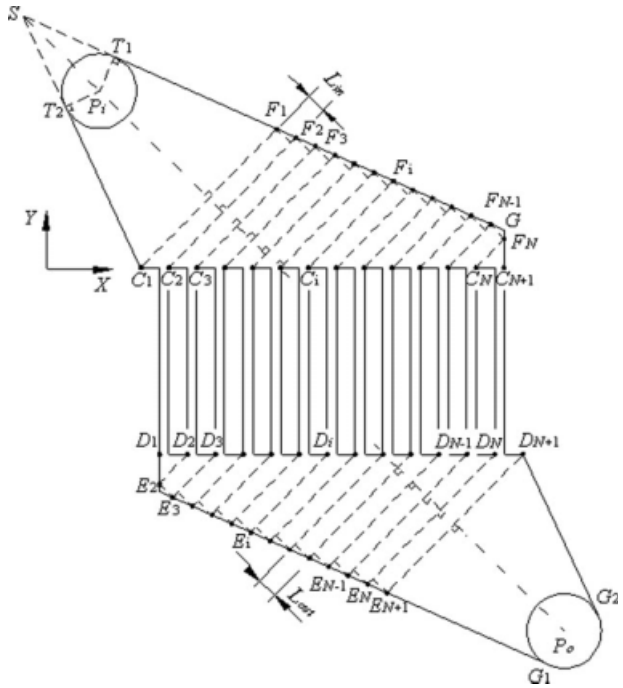

Figure 6. Division method of manifolds.

$$\begin{cases} X_{\mathrm{F}_i} = L_{\mathrm{m}} \\ Y_{\mathrm{F}_i} = k_{\mathrm{C}_i\mathrm{F}_i}(L_{\mathrm{m}} - X_{\mathrm{C}_i}) \end{cases} \tag{4}$$

$$X_{\mathrm{C}_i} = (i-1)\frac{L_{\mathrm{m}}}{N} \tag{5}$$

Here k represents the slope coefficient of each line segment.

Analysis of Flow Resistance Losses

Two categories of energy losses result from flow resistances during the flowing process: one is frictional losses caused by the wall shear in the pipe, and the other is singular losses caused by a change in the magnitude or the direction of the velocity vectors at the bends, enlargements, and contractions.

Frictional loss and pressure drop

In practice, the flow velocity in the microchannel is generally less than 10 m s^{-1} and the equivalent diameter of microchannel is no more than 500 μm so that the Reynolds number is less than 1000. Therefore, the flow pattern in microchannels is considered as a laminar flow.

According to Hagen-Poiseuille Equation, for a laminar flow in rectangular channels, the pressure drop ΔP due to frictional losses is defined as

$$\Delta P = \frac{32\mu L\lambda_{\mathrm{NC}}}{D_{\mathrm{H}}^2}U = R_{\mathrm{f}}U \tag{6}$$

where L is the channel length and D_{H} is hydraulic nominal diameter which is defined as below

$$D_{\mathrm{H}} = \frac{2WE}{W+E} \tag{7}$$

λ_{NC} is the non-circular coefficient,[9,10] of which magnitude depends on the ratio of channel depth E and width W as follows

$$\lambda_{\mathrm{NC}} = \frac{\frac{3}{2}}{\left[1-0.351\min\left(\frac{E}{W},\frac{W}{E}\right)\right]^2\left[1+\min\left(\frac{E}{W},\frac{W}{E}\right)\right]^2} \tag{8}$$

Substituting Eqs. 7 and 8 into Eq. 6, the following equation can be obtained.

$$R_{\mathrm{f}} = \frac{12\mu L}{\min^2(W,E)\left[1-0.351\min\left(\frac{E}{W},\frac{W}{E}\right)\right]^2} \tag{9}$$

Here R_{f} is called frictional resistance.

Singular loss and pressure drop

To analyze the catalogues of singular losses in the microchannel array model, the jth flow loop is selected from the model, as shown in Figure 7. The jth flow loop contains the jth approximate rectangular channel of the inlet manifold, the $(j-1)$th approximate rectangular channel of the outlet manifold, the $(j-1)$th and jth microchannel. Fluid in the flow loop flows in two different directions: the fluid from the jth approximate rectangular channel of the inlet manifold is split into two parts, one flow in the jth microchannel, and the other flow in the $(j+1)$th approximate rectangular channel of the inlet manifold, while the fluid from the $(j-1)$th microchannel and the $(j-2)$th approximate rectangular channel of the outlet manifold are combined into the $(j-1)$th approximate rectangular channel of the outlet manifold.

According to the analysis of the flow process of fluid in the jth flow loop, two kinds of singular losses[13] exist in the microchannel array model:

(1) As the fluid flows from the approximate rectangular channels of the inlet manifold to microchannels, there are three singular losses: diffuser loss $h_{j\mathrm{d}}$ caused by fluid

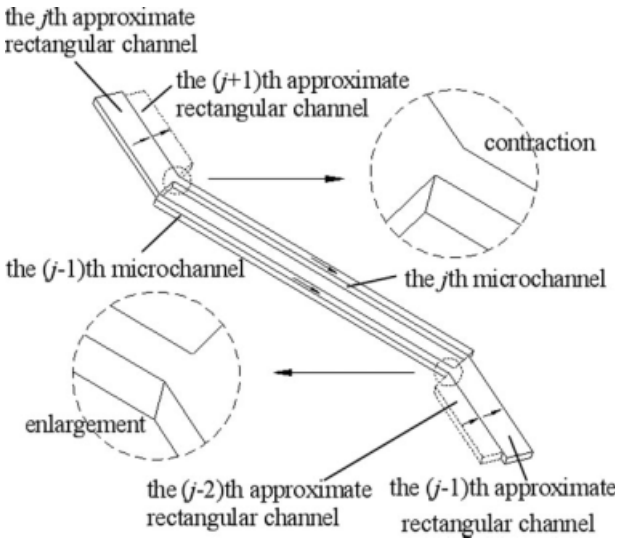

Figure 7. The *j*th flow loop.

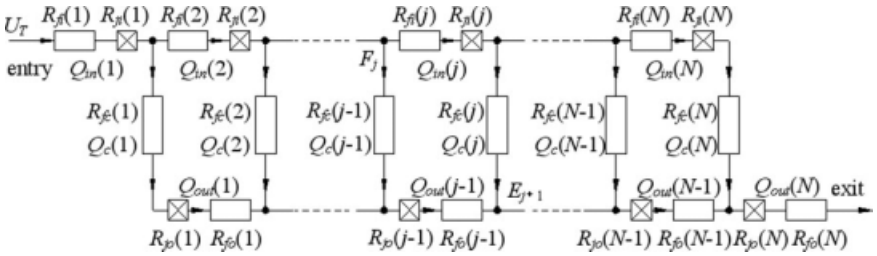

Figure 8. Simplified resistance network model.

splitting, contraction loss h_{jc} caused by the sudden contracting section and turning loss h_{jti}.

(2) When the fluid flows from microchannels to the approximate rectangular channels of the outlet manifold, the singular losses are composed of mixing loss h_{jm} caused by combination of two fluids with different velocities, enlargement loss h_{je} caused by the sudden increasing section and turning loss h_{jto}.

$\Delta P_{ji}(j)$ refers to the pressure drop caused by singular losses as the fluid flows from the jth approximate rectangular channels of the inlet manifold to the jth microchannels while $\Delta P_{jo}(j-1)$ refers to the pressure drop caused as the fluid flows from the $(j-1)$th microchannels to the $(j-1)$th approximate rectangular channels of the outlet manifold. They are defined, respectively, as follows.

$$\Delta P_{ji}(j) = \left(\zeta_{jd} + \zeta_{jc} + \zeta_{jti}\right)\frac{\rho}{2}U_{in}^2(j) = R_{ji}(j)U_{in}^2(j) \quad (j = 1,2,...,N) \tag{10}$$

$$\Delta P_{jo}(j-1) = \left(\zeta_{jm} + \zeta_{je} + \zeta_{jto}\right)\frac{\rho}{2}U_c^2(j-1) = R_{jo}(j-1)U_c^2(j-1) \quad (j = 2,3,\ldots,N+1) \tag{11}$$

where, ζ_{jd}, ζ_{jc}, ζ_{jti}, ζ_{jm}, ζ_{je}, and ζ_{jto} are singular resistance coefficients corresponding to singular losses h_{jd}, h_{jc}, h_{jti}, h_{jm}, h_{je}, and h_{jto}. R_{ji} and R_{jo} are called the singular resistances of entry end and exit end of the flow loop, respectively.

Simplified resistance network model

To distinctly analyze the relationships between the velocities and pressure drops in microchannels and approximate rectangular channels, the microchannel array model is equivalent to a simplified resistance network model, as depicted in Figure 8. In this model, the frictional resistances in the microchannels, the approximate rectangular channels of the inlet and outlet manifold are represented as electrical resistances $R_{fc}(j)$, $R_{fi}(j)$, and $R_{fo}(j)$ (j = 1, 2, …, N), respectively. The singular resistances of entry end and exit end of the flow loop are equivalent to $R_{ji}(j)$ and $R_{jo}(j)$ (j = 1, 2, …, N).

Transition chamber $T_1T_2C_1F_1$ of the inlet manifold and $D_{N+1}E_{N+1}G_1G_2$ of the outlet manifold are not considered in the simplified resistance network model, because they show no influences on the flow distribution among microchannels. To guarantee that the two models could be consistent to each other, according to the continuity equation of incompressible fluid, the entrance velocity U_T of the simplified resistance network model and the entrance velocity U_{in} of microchannel array model should satisfy the following relation.

$$U_{in}A_{pi} = U_T A_{T_1T_2C_1F_1} \tag{12}$$

where A_{pi} and $A_{T_1T_2C_1F_1}$ are the sectional areas of inlet P_i and the exit of transition chamber $T_1T_2C_1F_1$, respectively.

In the simplified resistance network model, the pressure drops of two ends (such as point F_j to E_{j+1} in Figure 8) in the diagonal line of each flow loop via two different flow channels are equal, therefore $N-1$ equations can be inferred as follows

$$\Delta P_{fi}(j) + \Delta P_{ji}(j) + \Delta P_{fc}(j) = \Delta P_{fc}(j-1) + \Delta P_{jo}(j-1) + \Delta P_{fo}(j-1) \quad (j = 2,3,\ldots,N) \tag{13}$$

According to the continuity equation of incompressible fluid, as shown in the simplified resistance network model, the relations of flow rates in the approximate rectangular channels of the inlet manifold and microchannels are defined as follows

$$Q_{in}(j) = Q_c(j) + Q_{in}(j+1) \quad (j = 1,2,\ldots,N-1) \tag{14}$$

$$Q_{in}(1) = Q_T \tag{15}$$

$$Q_{in}(N) = Q_c(N) \tag{16}$$

where Q_T is the total feed flow rate.

The relations of flow rates in the approximate rectangular channels of the outlet manifold and microchannels are defined as follows

$$Q_{out}(j) = Q_c(j) + Q_{out}(j-1) \quad (j = 2,3,\ldots,N) \tag{17}$$

$$Q_{out}(1) = Q_c(1) \tag{18}$$

The relationships between the channel velocity $U(j)$ and flow rate $Q(j)$ can be defined as follows

$$U(j) = \frac{Q(j)}{WE} \quad (j = 1,2,\ldots,N) \tag{19}$$

Substituting Eq. 19 into Eqs. 14–18, then $2N + 1$ equations are established about $U_{in}(j)$, $U_{out}(j)$, and $U_c(j)$. Together with Eq. 13, there are $3N$ independent equations. Since there

are $3N$ unknown variables about $U_{in}(j)$, $U_{out}(j)$, and $U_c(j)$ in the simplified resistance network model, they can be worked out by the combination of Eqs. 13–19.

Simplified calculation method of singular resistance coefficients

If all the structural parameters of the microchannel model are given, frictional resistance R_f can be calculated by Eq. 9, but the singular resistances cannot be solved according to Eqs. 10 and 11 unless the values of ζ_{jd}, ζ_{jc}, ζ_{jti}, ζ_{jm}, ζ_{je}, and ζ_{jto} are obtained. Equation 13 is established on the basis of $N-1$ flow loops and mainly relate to singular losses h_{jc}, h_{jti}, h_{je}, and h_{jto} in a flow loop, therefore the diffuser loss h_{jd} and mixing loss h_{jm} are ignored here.

The values of singular resistance coefficients in multiple microchannels are difficult even impossible to be exactly measured by experiments. Nowadays, the existed empirical equations of the singular resistance coefficients are just suitable for a single microchannel, there are no empirical equations for the complicated microchannel array proposed in this work. Even if the empirical equations of the complicated microchannel array were known, the calculations of singular resistance coefficients by empirical equations need to determine the velocities in the approximate rectangular channels and microchannels in advance. However, these values are unknown and require to be solved. Therefore, a simplified calculation method of singular resistance coefficients is proposed in this work.

Here, ζ_{jc} and ζ_{je} are calculated by the empirical equations of contraction loss and enlargement loss as follows, respectively.

$$\zeta_{jc}(j) = 0.5[1 - A_c(j)/A_{in}(j)] \quad (j = 2, 3, \ldots, N) \tag{20}$$

$$\zeta_{je}(j) = [1 - A_c(j-1)/A_{out}(j-1)]^2 \quad (j = 2, 3, \ldots, N) \tag{21}$$

where $A_c(j)$ represents the sectional area of the jth microchannel, $A_{in}(j)$ and $A_{out}(j-1)$ are the sectional areas of the jth approximate rectangular channel in the inlet manifold and the $(j-1)$th approximate rectangular channel in the outlet manifold, respectively.

Nowadays, few refers are provided for the calculations of ζ_{jti} and ζ_{jto} on the microscale. In this work, ζ_{jti} and ζ_{jto} are calculated by the empirical formula of the turning loss coefficients in the acute angle corner pipe with rectangular cross-section on the large scale[14] as follows, and then the validity are verified by the comparison of the calculation results of velocity distributions to the simulation ones.

$$\zeta_T = C_T A_T \zeta_M \tag{22}$$

where C_T is a function of the depth–width ratio E/W of channels, and A_T and ζ_M are the influence coefficient of turn angle δ of channels. The values of these three coefficients can be referred in Appendix B.

Results and Discussion

Velocity distribution profiles

Under different Reynolds numbers, the comparisons of the velocity distribution among microchannels simulated by Fluent and calculated by two methods of the theoretical model are shown in Figure 9. Results indicate that the two calculation methods accord with the Fluent's simulation under low Reynolds numbers, such as 0.6 and 6, which shows that the singular losses take little effects on the velocity distribution among microchannels. The velocity distribution appears symmetrical. Commenge et al.[9] considered that the centrosymmetry of the microchannel model was the cause of a symmetrical velocity distribution.

With larger Reynolds numbers, such as 60 and 300, the calculations considering singular losses also maintain consistence with the simulation one. The velocity distributions begin to be asymmetrical, and the values of velocities in the microchannels far away from the inlet are larger than that in the microchannels near the inlet. This trend becomes more obvious with the increasing Reynolds numbers. However, the velocity distributions obtained by the calculation which ignores singular losses still maintain symmetrical and begin to deviate from Fluent's simulation. The deviation becomes much larger with the increasing Reynolds numbers. As a result, the singular losses play an important role under large Reynolds numbers.

With further increasing Reynolds numbers, such as 600 and 3000, both calculation results, especially the one ignoring the singular losses, significantly deviate from the simulation one. This is because the pressure contours in the manifold become unparallel under large Reynolds numbers and hence results in unsuitable application of the theoretical model proposed based on parallel distributions of pressure contours.

From the comparison results of the velocity distributions among microchannels calculated by the theoretical model and simulated by Fluent, it can be concluded that the calculation of ζ_{js} and ζ_{jd} by the formula of the turning loss coefficients in the acute angle corner pipe with rectangular cross-section on the large scale are feasible under low Reynolds numbers.

Analysis of the effects of singular losses

The effects of singular losses under low Reynolds numbers are analyzed here by way of a function $\beta(j)$ of pressure drop proportion in each flow loop, which are defined below

$$\beta_i(j) = \frac{\Delta P_{fi}(j)}{\Delta P_{ji}(j)} \quad (j = 2, 3, \ldots, N) \tag{23}$$

$$\beta_o(j-1) = \frac{\Delta P_{fo}(j-1)}{\Delta P_{jo}(j-1)} \quad (j = 2, 3, \ldots, N) \tag{24}$$

where $\beta_i(j)$ and $\beta_o(j-1)$ represent the ratios of the pressure drop caused by frictional losses and singular losses in the inlet manifold and outlet manifold of the jth flow loop, respectively.

Table 2 shows the calculation results of pressure drop proportions with four different low Reynolds numbers. For all the flow loops, when the Reynolds number is very low, such as 0.6, the magnitudes of pressure drops in the inlet manifold and outlet manifold caused by frictional losses are 274–1748 and 65–253 times, respectively, as large as that caused

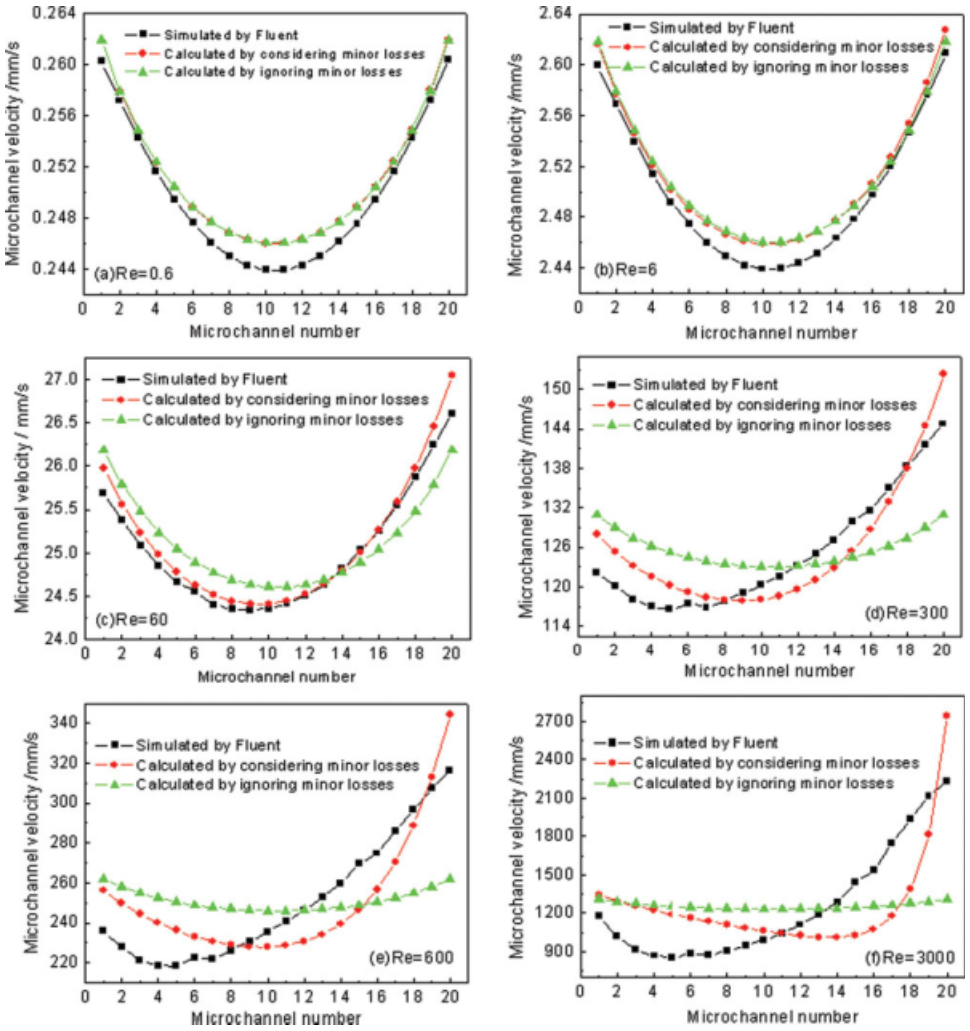

Figure 9. The comparisons of velocity distributions among microchannels calculated by two methods and simulated by Fluent under different Reynolds numbers.

[Color figure can be viewed in the online issue, which is available at www.interscience.wiley.com.]

Table 2. The Calculation of Pressure Drop Proportion in Each flow Loop

	$Re = 0.6$		$Re = 6$		$Re = 60$		$Re = 300$	
j	$\beta_i(j)$	$\beta_o(j-1)$	$\beta_i(j)$	$\beta_o(j-1)$	$\beta_i(j)$	$\beta_o(j-1)$	$\beta_i(j)$	$\beta_o(j-1)$
2	274.86	65.45	27.49	6.55	2.75	0.66	0.55	0.13
3	279.95	111.09	27.99	11.12	2.80	1.12	0.56	0.23
4	285.46	144.64	28.54	14.48	2.85	1.46	0.57	0.30
5	291.52	170.25	29.14	17.04	2.91	1.72	0.58	0.36
6	298.16	190.35	29.81	19.05	2.97	1.93	0.59	0.40
7	305.74	206.32	30.56	20.65	3.04	2.09	0.60	0.43
8	314.35	219.24	31.41	21.95	3.13	2.22	0.62	0.46
9	324.19	229.71	32.40	22.99	3.22	2.32	0.63	0.48
10	335.85	238.22	33.56	23.84	3.33	2.40	0.65	0.50
11	349.79	245.02	34.94	24.52	3.46	2.47	0.67	0.51
12	366.76	250.44	36.63	25.05	3.63	2.51	0.70	0.52
13	387.87	254.58	38.74	25.46	3.83	2.55	0.74	0.52
14	415.07	257.61	41.45	25.75	4.09	2.56	0.78	0.52
15	451.48	259.54	45.07	25.92	4.44	2.57	0.84	0.51
16	502.42	260.38	50.16	26.00	4.93	2.56	0.92	0.50
17	579.61	260.24	57.82	25.96	5.66	2.54	1.05	0.48
18	708.22	259.02	70.63	25.82	6.90	2.51	1.26	0.46
19	966.06	256.60	96.37	25.56	9.39	2.46	1.69	0.43
20	1747.97	252.93	173.91	25.17	16.89	2.40	3.00	0.40

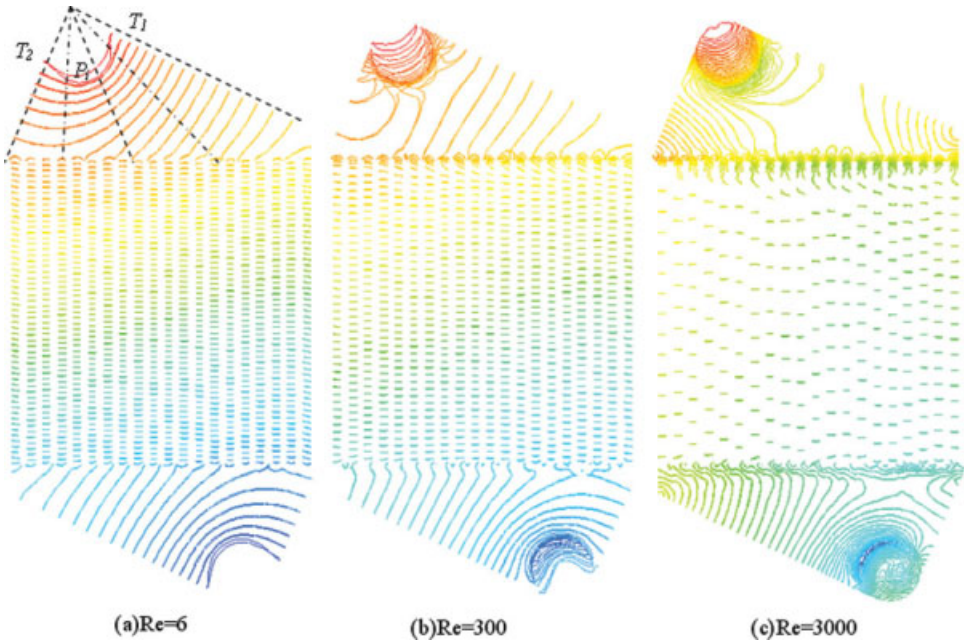

Figure 10. Pressure distributions in the acute angled triangle manifolds under different Reynolds numbers.

[Color figure can be viewed in the online issue, which is available at www.interscience.wiley.com.]

by singular losses. When the Reynolds number is equal to 6, the ratios turn to be 27.5–174 times and 6.6–25 times, respectively. Evidently, the pressure drops caused by singular losses are very small under low Reynolds numbers, leading to little effects on the calculations of theoretical model, as shown in Figures 9a, b.

However, with the increasing Reynolds numbers, such as 60, the ratios of two kinds of pressure drops are changed to 2.7–16.9 times in the inlet manifold and 0.6–2.4 times in the outlet manifold, which indicates that the ratios of pressure drops decrease. If singular losses are ignored at the time, the calculation results will deviate from the original model, as shown in Figure 9c. And the deviation will be much larger with the increasing Reynolds numbers. When the Reynolds number is equal to 300, the ratios of two kinds of pressure drops are 0.5–3 times in the inlet manifold and 0.13–0.4 times in the outlet manifold, respectively. And the pressure drop caused by singular losses is nearly the same as the one caused by frictional losses, even more than the latter. Ignoring singular losses during the calculations will result in incorrect velocity distributions, as shown in Figure 9d.

Therefore, the governing factor for ignoring the singular losses under low Reynolds numbers is that the pressure drops caused by singular losses must be considerably small. On the basis of above analysis, so-called "considerably small" here means that the pressure drops caused by frictional losses should be three times larger than that caused by singular losses in each flow loop.

The application scope of the theoretical model

Figure 10 shows the distributions of pressure contours in the acute triangle manifolds under different Reynolds numbers. For the low Reynolds numbers, such as 6, the pressure contours around the inlet appear to be curving. The distribution of pressure contours becomes somewhat disordered when $Re = 300$. And it becomes more disordered with the increasing Reynolds numbers. Obviously, the distributions of pressure contours in the acute triangle manifold are quite different from the one in the obtuse angled triangle manifolds. The theoretical model is established on the premise of parallel distributions of pressure contours, therefore the proposed theoretical model is not suitable for the microchannel array model with acute triangle manifolds. Otherwise, the obtained velocity distribution will deviate from the realities. Figure 11 shows the comparison of velocity distribution simulated by Fluent and the calculation by the theoretical model considering singular losses for the microchannel array with acute triangle manifolds. Here, U_{m} refers to the average velocity of microchannels as defined below.

$$U_{\mathrm{m}} = \frac{1}{N}\sum_{i=1}^{N} U_{\mathrm{c}}(j) \quad (j = 1, 2, \ldots, N) \tag{25}$$

Optimization of the manifold shape

For qualitatively estimating the quality of velocity distributions for different microchannel models, a parameter $\sigma_U\%$ is defined as below. Smaller $\sigma_U\%$ suggests more uniform flow distributions.

$$\sigma_U\% = 100\sqrt{\frac{1}{N}\sum_{j=1}^{N}\left(\frac{U_{\mathrm{c}}(j)}{\mathrm{U_m}} - 1\right)^2} \tag{26}$$

When the microchannel structural parameters are given, the velocity distributions among microchannels are mainly dominated by the manifold shape. From the point of

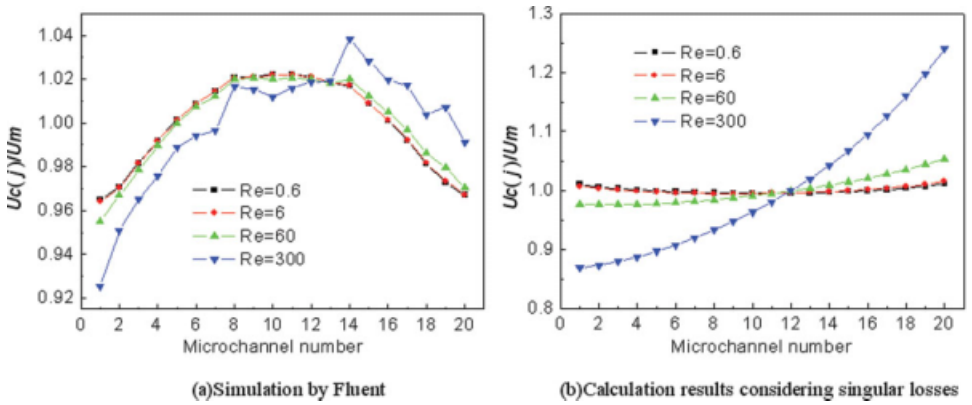

Figure 11. Velocity distributions among microchannels with acute triangle manifolds under different Reynolds numbers.

[Color figure can be viewed in the online issue, which is available at www.interscience.wiley.com.]

manifold design, the manifold shape are determined by the position (X_{pi}, Y_{pi}) and the radius R_{pi} of the inlet (or outlet) as well as the side length H of the manifold. Therefore, the magnitudes of X_{pi}, Y_{pi}, R_{pi}, and H play an important role in the velocity distributions among microchannels. However, their values are usually limited within certain ranges due to the sheet dimension or fabrication constrains. Assume that their ranges are defined as follows, respectively.

$$\min X_{pi} \le X_{pi} \le \max X_{pi} \tag{27}$$

$$\min Y_{pi} \le Y_{pi} \le \max Y_{pi} \tag{28}$$

$$\min R_{pi} \le R_{pi} \le \max R_{pi} \tag{29}$$

$$\min H \le H \le \max H \tag{30}$$

The manifold shape is changed with the variety of X_{pi}, Y_{pi}, R_{pi}, and H within their limits. During the optimization of the manifold shape, all the $\sigma_U\%$ values of different manifold shapes are worked out, and the shape corresponding to the minimum value of $\sigma_U\%$ is the best one. The flowchart of the optimization procedure is shown in Figure 12.

However, numerous manifold shapes can be obtained with the simultaneous varieties of the four manifold structural parameters. It requires nevertheless lengthy time to reach the optimal shape. Therefore, only one of the structural parameters is usually chosen to optimize in practice while other parameters maintain constant. Here, the microchannel array model in Table 1 is also selected as example. Assume that the entrance velocity is 1 mm s^{-1} and the values of Y_{pi}, R_{pi}, and H are invariant, the value of X_{pi} is increased stepwise from -4 to 2, with the increment of 0.1. Figure 13 shows

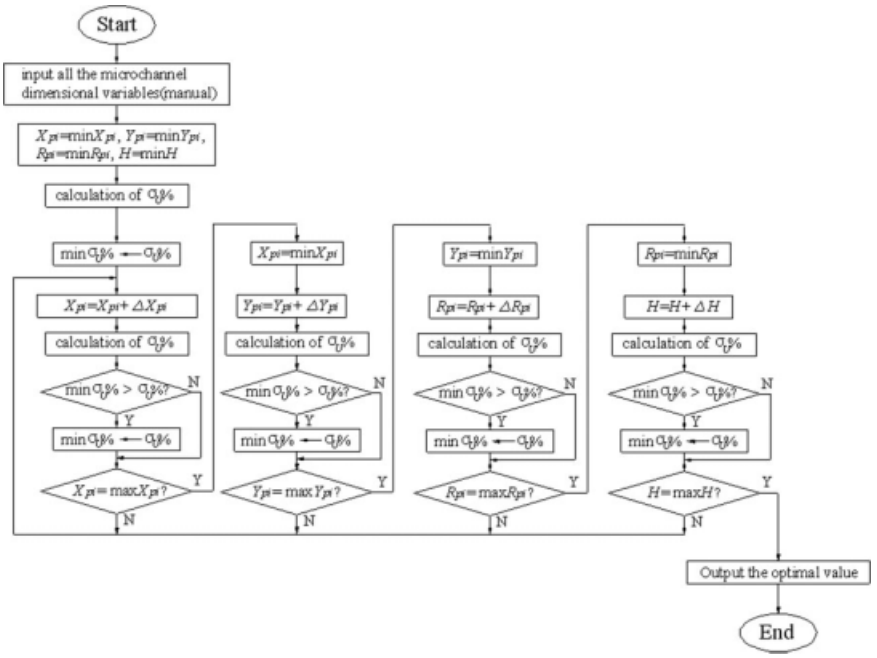

Figure 12. The flowchart of the optimization procedure.

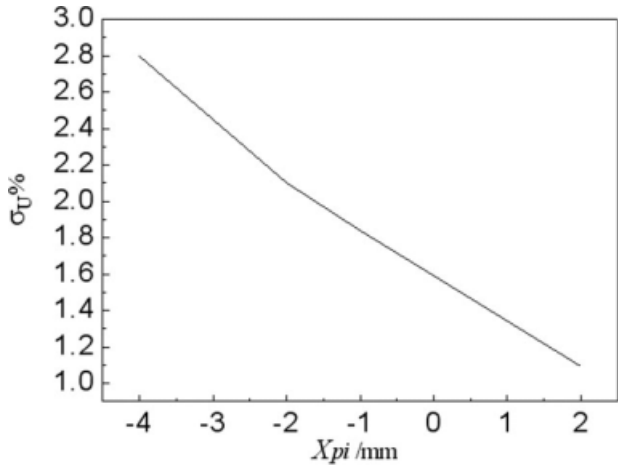

Figure 13. The relation between the σ_U% and X_{pi}.

how the different σ_U% values vary with different X_{pi}. It indicates that the velocity distributions among microchannels get more uniform with larger X_{pi}, and the velocity distributions among the microchannels with the right triangle manifolds($X_{pi} = 2$) is much more uniform than that of the corresponding one with obtuse angled manifolds ($X_{pi} < 2$).

Conclusions

The two calculation methods, considering and ignoring singular losses accord with the Fluent's simulation under low Reynolds numbers, but with larger Reynolds numbers, the calculation ignoring singular losses begins to deviate from the simulation by Fluent and the one considering singular losses also maintain consistence with the simulation. The singular losses can be ignored during the calculation as the frictional pressure drops are three times larger than the singular pressure drops in each flow loop.

With large Reynolds numbers, the calculation results seriously deviate from the simulation due to unparallel distributions of the pressure contours in the manifold. The pressure contours in acute triangle manifolds appear to be curving around the inlet under low Reynolds numbers. The theoretical model, which is established on the premise of parallel distributions of pressure contours, is only suitable for the calculation of velocity distributions among microchannels with obtuse angled or right triangle manifolds under low Reynolds numbers.

The manifold optimization results indicate that the velocity distribution among microchannels with right triangle manifolds is much more uniform than that of the corresponding one with obtuse angled manifolds when they have the same microchannel structural parameters and Y_{pi}, R_{pi}, and H.

Acknowledgments

This research was supported by the National Nature Science Foundation of China, Project No. 50805052, the Natural Science Foundation of Guangdong Province, Project No. 8451064101000320 and the Doctoral Program of Ministry of Education of China, Project No. 200805611089.

Notation

A = sectional area of channels, m^2
A_{pi} = the sectional area of the inlet, m^2
A_T = influence coefficient of turn angle of channels
C_T = influence coefficient of depth–width ratio of channels
D_H = hydraulic nominal diameter, m
E = channel thickness, m
H_{in} = length of GC_{N+1}, m
h_{jc} = contraction loss
h_{jd} = diffuser loss
h_{je} = enlargement loss
h_{jti} = turning loss in the inlet manifold
h_{jto} = turning loss in the outlet manifold
h_{jm} = mixing loss
i, j = integer variable
k = Slope coefficient of line segment
L = channel length/segment length, m
L_m = length of C_1C_{N+1}, m
max = maximum value
min = minimum value
N = microchannel number
ΔP = pressure drop, Pa
$\Delta P_{fc}(j)$ = frictional pressure drop in the jth microchannel, Pa
$\Delta P_{fi}(j)$ = frictional pressure drop in the jth approximate rectangular channel of the inlet manifold, Pa
$\Delta P_{fo}(j)$ = frictional pressure drop in the jth approximate rectangular channel of the outlet manifold, Pa
$\Delta P_{ji}(j)$ = singular pressure drop of entry end of the jth flow loop, Pa
$\Delta P_{jo}(j-1)$ = singular pressure drop of exit end of the jth flow loop, Pa
Q_T = total feed flow rate, $m^3\ s^{-1}$
$Q(j)$ = flow rate of the jth channels, $m^3\ s^{-1}$
R_f = Frictional resistance, Pa s m^{-1}
$R_{fc}(j)$ = frictional resistance in the jth microchannel, Pa s m^{-1}
$R_{fi}(j)$ = frictional resistance in the jth approximate rectangular channel of the inlet manifold, Pa s m^{-1}
$R_{fo}(j)$ = frictional resistance in the jth approximate rectangular channel of the outlet manifold, Pa s m^{-1}
$R_{ji}(j)$ = singular resistance of entry end of the jth flow loop, Pa s m^{-2}
$R_{jo}(j-1)$ = singular resistance of entry end of exit end of the jth flow loop, Pa s m^{-2}
R_{pi} = Radius of the inlet, m
U = fluid velocity, m s^{-1}
U_{in} = entrance velocity of microchannel array model, m s^{-1}
U_m = average velocity of microchannels, m s^{-1}
U_T = Entrance velocity of the simplified resistance network model, m s^{-1}
W = channel width, m
X = horizontal coordinate, m
X_{pi} = horizontal coordinate of the inlet, m
Y = vertical coordinate, m
Y_{pi} = vertical coordinate of the inlet, m

Subscripts

c = microchannel
in, i = inlet manifold
out, o = outlet manifold

Greek letters

λ_{NC} = non-circular coefficient
μ = viscosity (Pa s)
β = pressure drop proportion
ρ = fluid density (kg m^{-3})
δ = turn angle of channels (°)
σ_U% = estimating parameters of velocity distributions
ζ_{jc} = contraction loss coefficient
ζ_{jd} = diffuser loss coefficient
ζ_{je} = enlargement loss coefficient
ζ_{jti} = turning loss coefficient in the inlet manifold
ζ_{jto} = turning loss coefficient in the outlet manifold
ζ_{jm} = mixing loss coefficient
ζ_M = a factor determined by related formula
ζ_T = turning loss coefficients in the acute angle corner pipe with rectangular cross-section

Literature Cited

1. Miyazaki M, Maeda H. Microchannel enzyme reactors and their applications for processing. *Trends Biotechnol*. 2006;24:463–470.
2. Pattekar AV, Kothare MV. A microreactor for hydrogen production in micro fuel cell applications. *J Microelectromech Syst*. 2004;13:7–18.
3. Pattekar AV, Kothare MV. A Microreactor for In Situ Hydrogen Production by Catalytic Methanol Reforming. Proceedings of the 5th International Conference on Microreaction Technology (IMRET 5). Strasbourg, France, 2001.
4. Kikas T, Zhang H, Bardenshteyn I, Ejimofor C, Puri P, Philips C, Fedorov AG. Feedstock for Micro Fuel Cells: Efficient Hydrogen Production in the Reverse-Flow Autothermal Catalytic Microreactors. International Symposium on Micro/Nanoscale Energy Conversion, MECT-02, International Centre for Heat and Mass Transfer. Antalya, Turkey, 2002.
5. Ganley JC, Seebauer EG, Masel RI. Development of a microreactor for the production of hydrogen from ammonia. *J Power Sources*. 2004;137:53–61.
6. Zheng N, Seebauer EG, Masel RI. Effects of microreactor geometry on performance: differences between posted reactors and channel reactors. *Ind Eng Chem Res*. 2005;44:4267–4271.
7. Martin PM, Matson DW, Bennett WD, Stewart DC, Lin Y. Laser Micromachined and Laminated Icrofluidic Components for Miniaturized Thermal, Chemical and Biological Systems. SPIE Conference Proceedings, Design, Test, and Micro-fabrication of MEMS and MOEMS. Paris, France, 1999:826–833.
8. Park GG, Yima SD, Yoon YG, Lee WY, Kima CS, Seo DJ, Eguchi K. Hydrogen production with integrated microchannel fuel processor for portable fuel cell systems. *J Power Sources*. 2005;145:702–706.
9. Commenge JM, Falk L, Corriou JP, Matlosz M. Optimal design for flow uniformity in microchannel reactors. *AIChE J*. 2002;48:345–357.
10. Amador C, Gavriilidis A, Angeli P. Flow distribution in different microreactor scale-out geometries and the effect of manufacturing tolerances and channel blockage. *Chem Eng J*. 2004;101:379–390.
11. Tonomura O, Tanaka S, Noda M, Kano M, Hasebe S, Hashimoto I. CFD-based optimal design of manifold in plate-fin microdevices. *Chem Eng J*. 2004;101:397–402.
12. Judy J, Maynes D, Webb BW. Characterization of frictional pressure drop for liquid flows through microchannels. *Int J Heat Mass Transfer*. 2002;45:3477–3489.
13. Boersma RJ, Sammes NM. Distribution of gas flow in internally manifolded solid oxide fuel-cell stacks. *J Power Sources*. 1997;66:41–45.
14. Hua Sh, Yang X. *Practical Handbook of Fluid Resistances*, 1st ed. Beijing: Defence Industry Press, 1985: 305–358.

Appendix A

Calculation method of the dimensions of approximate rectangular channels

Take the inlet manifold for sample to present the calculation method of the dimensions of approximate rectangular channels with given parameters, such as X_{pi}, Y_{pi}, R_{pi}, L_{m}, and H_{in}. The calculation method of the outlet manifold is similar to that of the inlet manifold. Some auxiliary lines are drawn to work out the length and width of each approximate rectangular channel, as shown in Figure A1. First connect G and C_1 to P_i, respectively. Draw GG_1 parallel to C_1C_{N+1} through G. Then draw P_iG_3 perpendicular to C_1C_{N+1} through P_i, intersecting to GG_1 at G_1 and C_1C_{N+1} at G_3.

So, the linear equation of SG can be represented as follows

$$y = k_{\mathrm{SG}}(x - L_{\mathrm{m}}) + H_{\mathrm{in}} \tag{A1}$$

Here, k_{SG} is the slope coefficient of SG, which is defined as below

$$k_{\mathrm{SG}} = \mathrm{tg}(108^{\circ} - \angle \mathrm{T_1GG_1}) \tag{A2}$$

where

$$\angle \mathrm{T_1GG_1} = \angle \mathrm{T_1GP}_i + \angle P_i\mathrm{GG_1} \tag{A3}$$

$$\angle \mathrm{T_1GP}_i = \arcsin\frac{L_{\mathrm{T_1P}_i}}{L_{\mathrm{GP}_i}} = \arcsin\frac{\mathrm{R_{pi}}}{L_{\mathrm{GP}_i}} \tag{A4}$$

$$\angle P_i\mathrm{GG_1} = \arcsin\frac{L_{\mathrm{P}_iG_1}}{L_{\mathrm{GP}_i}} = \arcsin\frac{Y_{\mathrm{pi}}H_{\mathrm{in}}}{L_{\mathrm{GP}_i}} \tag{A5}$$

The length of GP_i is obtained as follows

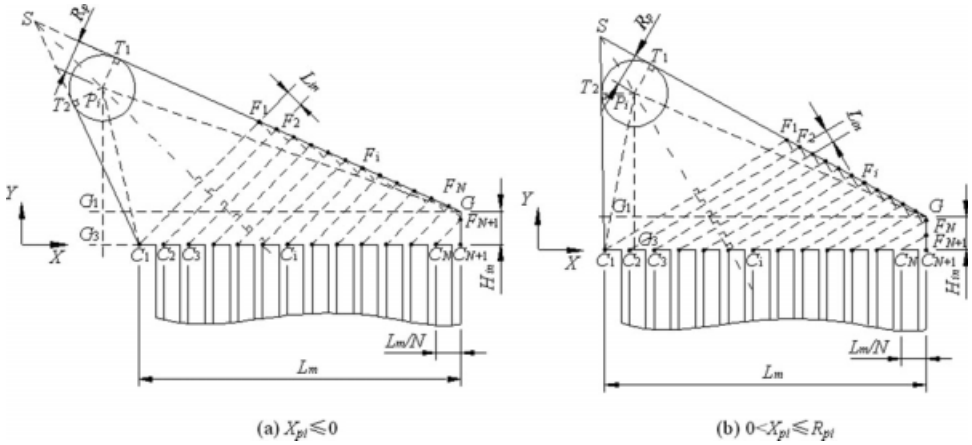

Figure A1. Auxiliary lines for calculating the lengths and widths of approximate rectangular channels.

$$L_{\mathrm{GP}_i} = \sqrt{(X_{\mathrm{pi}} - L_{\mathrm{m}})^2 + (Y_{\mathrm{pi}} - H_{\mathrm{in}})^2} \tag{A6}$$

Similarly, the linear equation of SC_1 can be defined as

$$y = k_{\mathrm{SC}_1} x \tag{A7}$$

Here, k_{SC_1} represents the slope coefficient of SC_1.

When the center of the inlet P_i locates at the left of the axis Y or on the axis Y, i.e., $X_{\mathrm{pi}} \leq 0$ as shown in Figure A1a, the magnitude of $\angle T_2C_1G_3$ and k_{SC_1} are respectively defined as

$$\angle \mathrm{T_2C_1G_3} = \angle \mathrm{P}_i\mathrm{C_1G_3} - \angle \mathrm{T_2C_1P}_i \tag{A8}$$

$$k_{\mathrm{SC}_1} = \mathrm{tg}(180^\circ - \angle \mathrm{T_2C_1G_3}) \tag{A9}$$

The magnitude of $\angle T_2C_1G_3$ and k_{SC_1} are obtained as follows while $0 < X_{\mathrm{pi}} \leq R_{\mathrm{pi}}$, as presented in Figure A1b.

$$\angle \mathrm{T_2C_1G_3} = \angle \mathrm{P}_i\mathrm{C_1G_3} + \angle \mathrm{T_2C_1P}_i \tag{A10}$$

$$k_{\mathrm{SC}_1} = \mathrm{tg}\angle \mathrm{T_2C_1G_3} \tag{A11}$$

where

$$\angle \mathrm{T_2C_1P}_i = \arcsin\frac{L_{\mathrm{T_2P}_i}}{L_{\mathrm{C_1P}_i}} = \arcsin\frac{R_{\mathrm{pi}}}{L_{\mathrm{C_1P}_i}} \tag{A12}$$

$$\angle \mathrm{P}_i\mathrm{C_1G_3} = \arcsin\frac{L_{\mathrm{G_3P}_i}}{L_{\mathrm{C_1P}_i}} = \arcsin\frac{Y_{\mathrm{pi}}}{L_{\mathrm{C_1P}_i}} \tag{A13}$$

The length of C_1P_i is defined as follows

$$L_{\mathrm{C_1P}_i} = \sqrt{X_{\mathrm{pi}}^2 + Y_{\mathrm{pi}}^2} \tag{A14}$$

The coordinate (X_S, Y_S) of S can be worked out by the combination of Eqs. A1 and A7.

$$X_{\mathrm{s}} = \frac{k_{\mathrm{SG}} \cdot L - H_{\mathrm{in}}}{k_{\mathrm{SG}} - k_{\mathrm{SC}_1}} \tag{A15}$$

$$Y_{\mathrm{s}} = \frac{(k_{\mathrm{SG}} \cdot L - H_{\mathrm{in}})k_{\mathrm{SC}_1}}{k_{\mathrm{SG}} - k_{\mathrm{SC}_1}} \tag{A16}$$

The slope coefficient of SP_i can be defined as

$$k_{\mathrm{SP}_i} = \frac{Y_{\mathrm{pi}} - Y_{\mathrm{s}}}{X_{\mathrm{pi}} - X_{\mathrm{s}}} \tag{A17}$$

Then the slope coefficient of C_iF_i (i = 1, 2, …, N) is obtained

$$k_{\mathrm{C}_i\mathrm{F}_i} = -\frac{1}{k_{\mathrm{SP}_i}} \quad (i = 1, 2, \ldots, N) \tag{A18}$$

The magnitude of $\angle F_iC_iC_{N+1}$ is defined as

$$\angle \mathrm{F}_i\mathrm{C}_i\mathrm{C}_{N+1} = \arctan k_{\mathrm{C}_i\mathrm{F}_i} \quad (i = 1, 2, \ldots, N) \tag{A19}$$

It is assumed that microchannels are uniformly distributed, so the sum of each microchannel width and interval is L_m/N. So, the length of each approximate rectangular channel can be worked out.

$$L_{\mathrm{in}} = L_{\mathrm{m}}/N \cdot \sin\angle \mathrm{F}_i\mathrm{C}_i\mathrm{C}_{N+1} \tag{A20}$$

The equation of C_iF_i is defined as

$$y = k_{\mathrm{C}_i\mathrm{F}_i}(x - X_{\mathrm{C}_i}) \quad (i = 1, 2, \ldots, N) \tag{A21}$$

where

$$X_{\mathrm{C}_i} = (i-1)\frac{L_{\mathrm{m}}}{\mathrm{N}} \quad (i = 1, 2, \ldots, N+1) \tag{A22}$$

The coordinate of F_i (i = 1, 2, …, N) are depended on the location of the inlet and on the length H_{in}. When points F_i (i = 1, 2, …, N) are on the line SG, combine the Eq. A1 with Eq. A21 to solve the coordinate X_{F_i},Y_{F_i} of F_i (i = 1, 2, …, N) as follows

$$X_{\mathrm{F}_i} = \frac{k_{\mathrm{SG}} \cdot L_{\mathrm{m}} - k_{\mathrm{C}_i\mathrm{F}_i} \cdot (i-1)\frac{L_{\mathrm{m}}}{N} - H_{\mathrm{in}}}{k_{\mathrm{SG}} - k_{\mathrm{C}_i\mathrm{F}_i}} \tag{A23}$$

$$Y_{\mathrm{F}_i} = \frac{-k_{\mathrm{SG}}k_{\mathrm{C}_i\mathrm{F}_i}(i-1)\frac{L_{\mathrm{m}}}{N} + k_{\mathrm{SG}}k_{\mathrm{C}_i\mathrm{F}_i}L_{\mathrm{m}} - k_{\mathrm{C}_i\mathrm{F}_i}H_{\mathrm{in}}}{k_{\mathrm{SG}} - k_{\mathrm{C}_i\mathrm{F}_i}} \tag{A24}$$

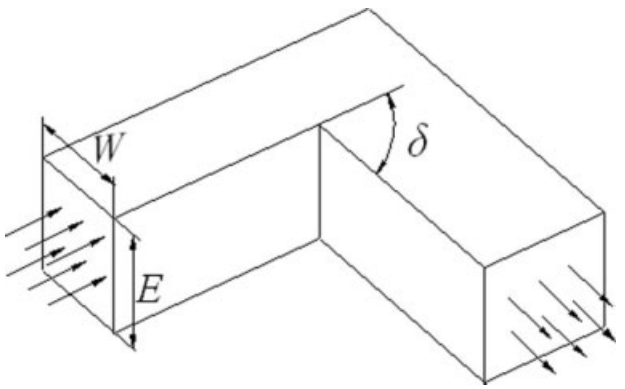

Figure B1. The schematic diagram of fluid flows in the acute angle corner pipe with rectangular cross-section.

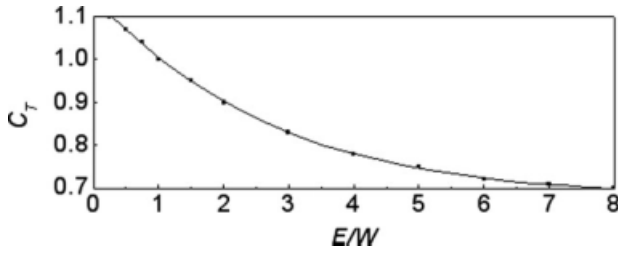

Figure B2. The curve diagram of $C_T = f(E/W)$.

If the value of X_{F_i} obtained by Eq. A23 is larger than that of L_m, it represents that point F_i ($i = 1, 2, \ldots, N$) are on the line GC_{N+1}, and the coordinate (X_{F_i}, Y_{F_i}) of F_i ($i = 1, 2, \ldots, N$) are as follows

$$X_{F_i} = L_m \tag{A25}$$

$$Y_{F_i} = k_{C_iF_i}(L_m - X_{C_i}) \tag{A26}$$

Since Y_{C_i} ($i = 1, 2, \ldots, N$) is equal to zero, the widths C_iF_i ($i = 1, 2, \ldots, N$) of approximate rectangular channels can be worked out as follows

$$L_{C_iF_i} = \sqrt{(X_{C_i} - X_{F_i})^2 + Y_{F_i}^2} \quad (i = 1, 2, \ldots, N) \tag{A27}$$

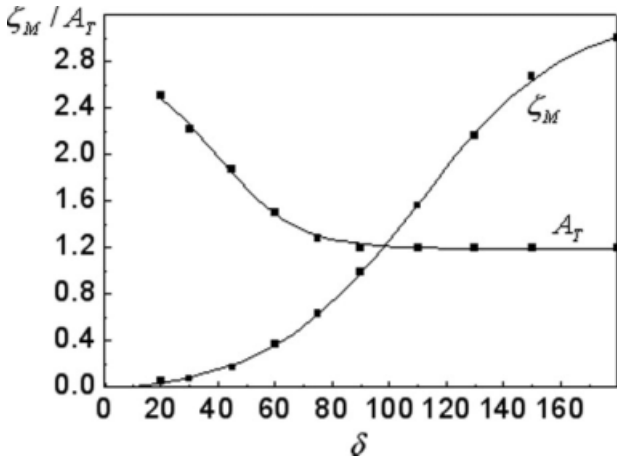

Figure B3. The curve diagram of $\zeta_M = f(\delta)$ and $A_T = f(\delta)$.

Appendix B

The turning loss coefficients in the acute angle corner pipe with rectangular cross-section on the large scale

Figure B1 shows the schematic diagram of fluid flows in the acute angle corner pipe with rectangular cross-section. The turning loss is related to the depth–width ratio E/W and the turn angle δ. In the formula, C_T relates to E/W and can be determined by Figure B2. A_T and ζ_M relate to δ and can be determined by Figure B3.

Manuscript received July 6, 2008, revision received Oct. 14, 2008, and final revision received Jan. 2, 2009.